

RESEARCH ARTICLE | APRIL 05 2024

Improved crystallographic order of ScAlN/GaN heterostructures grown at low temperatures under metal rich surface conditions ^F

Keisuke Motoki ^{ID}; Zachary Engel ^{ID}; Timothy M. McCrone ^{ID}; Huijin Chung ^{ID}; Christopher M. Matthews ^{ID}; Sangho Lee ^{ID}; Emily N. Marshall ^{ID}; Aheli Ghosh ^{ID}; Amanda Tang ^{ID}; W. Alan Doolittle [✉] ^{ID}

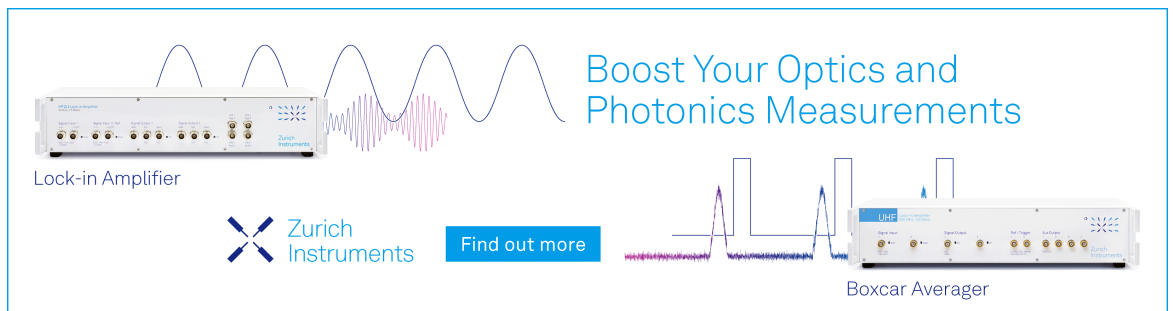
 Check for updates

J. Appl. Phys. 135, 135105 (2024)

<https://doi.org/10.1063/5.0176344>



View
Online


Export
Citation



Boost Your Optics and Photonics Measurements

Lock-in Amplifier

 Zurich Instruments

[Find out more](#)

Boxcar Averager

Improved crystallographic order of ScAlN/GaN heterostructures grown at low temperatures under metal rich surface conditions

Cite as: J. Appl. Phys. **135**, 135105 (2024); doi: [10.1063/5.0176344](https://doi.org/10.1063/5.0176344)

Submitted: 12 September 2023 · Accepted: 6 March 2024 ·

Published Online: 5 April 2024



Keisuke Motoki,  Zachary Engel,  Timothy M. McCrone,  Huijin Chung,  Christopher M. Matthews,  Sangho Lee,  Emily N. Marshall,  Aheli Ghosh,  Amanda Tang,  and W. Alan Doolittle^{a)} 

AFFILIATIONS

School of Electrical and Computer Engineering, Georgia Institute of Technology, Atlanta, Georgia 30332, USA

^{a)}Author to whom correspondence should be addressed: alan.doolittle@ece.gatech.edu

ABSTRACT

Sc_{0.18}Al_{0.82}N/GaN with state-of-the-art x-ray diffraction figures of merit grown by metal modulated epitaxy under metal-rich conditions and a low substrate temperature of 400 °C is demonstrated to have improved crystalline order [250 arc sec for the (0002) reflection and 469 arc sec for the (10 $\bar{1}$ 5)] compared to a previous state-of-the-art sample grown at a more conventional temperature of 650 °C. While both samples show a columnar structure, the higher substrate temperature sample has a good symmetric rocking curve (RC) of 229 arc sec, but unlike the lower temperature sample, the RC of the (10 $\bar{1}$ 5) asymmetric reflection could not be measured, indicating a more columnar structure common among ScAlN films. Local lattice constant maps (LLCMs) from 4D-STEM depict abrupt strain relaxation within ~2 nm from the ScAlN/GaN interface for the sample grown at T_{sub} = 400 °C. Since these LLCMs suggest a lattice mismatch in the a-lattice constant, and since the films show a sudden roughening, the composition for lattice match to GaN may be less than the accepted 18%–20% Sc, consistent with the average GaN lattice match from lattice constant values reported in the literature of 12%. Compared to traditional III-Nitrides, ScAlN films have substantially more screw and mixed-type threading dislocations, suggesting substantial shear forces that result in significant twist and distortion leading to orthorhombic diffraction patterns as viewed from plan-view TEM in the T_{sub} = 650 °C sample. These results offer the possibility of ScAlN integration into low-thermal-budget processes including CMOS but further indicate that structural understanding of ScAlN remains lacking.

© 2024 Author(s). All article content, except where otherwise noted, is licensed under a Creative Commons Attribution (CC BY) license (<https://creativecommons.org/licenses/by/4.0/>). <https://doi.org/10.1063/5.0176344>

INTRODUCTION

Wurtzite ScAlN is attractive due to its ferroelectric behavior and high spontaneous and piezoelectric polarization^{1–4} for application in acoustic wave devices, high electron mobility transistors (HEMTs), non-linear optics, and devices requiring robustness in high-temperature and high-radiation environments.^{1–4} Although, as shown in Fig. 1,^{5–14} ScAlN's lattice constants vary widely in the literature, especially when various synthesis methods are considered, it is generally considered to be lattice-matched to GaN when it is composed of approximately 18%–20% Sc.^{15–17} This literature assumption does not correspond with the numerical fit for GaN's lattice constant ($a = 3.189$ Å), which occurs in these data at ~12% Sc. We also note that during the growth of Sc_{0.18}Al_{0.82}N, RHEED often indicates a sudden onset of roughening, suggesting that the

film is relaxing when it reaches a critical thickness. As shown in Fig. 1, the lattice constant ratio, c/a , dramatically changes with increasing Sc concentration, resulting in enhanced polarization and piezoelectric properties. ScAlN's significant spontaneous polarization coefficients allow for the generation of two-dimensional electron gas (2DEG) densities as high as approximately 6×10^{13} cm⁻², even when it is lattice-matched to GaN, where the piezoelectric polarization does not influence the sheet charge.^{16,18} Among fabrication methods, radio frequency (RF) sputtering typically produces well-oriented polycrystalline ScAlN films with large defect densities suitable for acoustic devices, but lowering device performance for electronic devices.^{19–23} For most of the reports showing ScAlN films grown in molecular beam epitaxy (MBE), nitrogen-rich conditions prone to surface roughening are used to avoid the secondary intermetallic phases known to precipitate out under metal-rich conditions.²⁴

25 April 2024 10:41:07

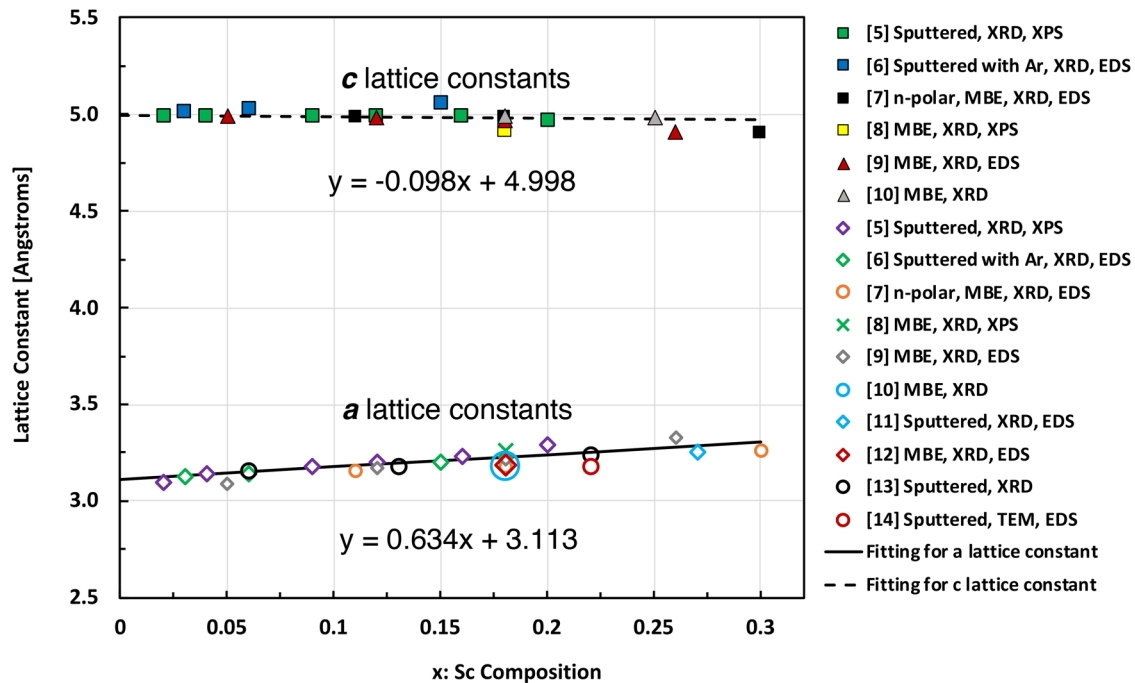


FIG. 1. Experimentally measured *a* and *c* lattice constants of $\text{Sc}_x\text{Al}_{1-x}\text{N}$ from literature surveys.^{5–14} The reference number, the synthesis methods, and the measurement equipment are indicated in the explanatory notes.

To reduce the surface roughening, incorporating AlN and/or AlGa_N interlayers to facilitate smooth HEMT barrier-channel interfaces has been studied.^{3,25–27} Likewise, incorporating an AlN interlayer reduces random alloy scattering. However, it is more beneficial to have direct contact with ScAlN to GaN due to its larger polarization discontinuity than Al(Ga)N/GaN.

Metal-rich growth is chemically preferred for the growth of III-nitrides in MBE as it promotes enhanced diffusion of adatoms on the surface and enables high 2D electron densities. Metal-rich traditional and cyclic low temperature forms (such as metal modulated epitaxy—MME) of III-nitride MBE are known to improve surface smoothness and interface roughness.^{28–32} However, because of the additional challenges due to the unintended incorporation of intermetallic Al_xSc_y and observation of rock-salt phases when attempting to grow ScAlN under metal-rich conditions,^{8,18,25} metal-rich growth has mostly been avoided in prior studies. Metal-rich ScAlN grown by MBE using Ga as a pseudo-surfactant shows promise, but this approach leads to the formation of a quaternary ScAlGa_N alloy since Ga is soluble in ScAlN.³³ In another report, Frei *et al.* achieved close to the theoretical 2DEG density without using the AlN/AlGa_N interlayer, but the film includes a metallic secondary phase that would make it hard to use the film for devices.¹⁸ Achieving phase-pure ScAlN under metal-rich MBE remains a challenge with only one successful report to our knowledge.²⁴

ScAlN was grown directly on GaN with spectacular interface smoothness by using MME, an MBE technique in which metal sources are periodically shuttered while active nitrogen is

continuously provided.²⁴ By periodically shuttering the metal source, MME can control the growth surface by making the surface metal-rich while the shutter is open and nitrogen-rich while the shutter is closed, allowing nitrogen to consume the available metal atoms before the shutter opens again. Using this growth mechanism, MME has demonstrated high-quality, single-phase InGa_N, AlIn_N, AlGa_N, and ScAlN films by utilizing III/V ratios well over stoichiometry but total metal doses that inhibit surface segregation, thus preventing phase separation and in ScAlN's case, intermetallic secondary phases.^{29,34–38} MME enables the precise control of metal adlayer buildup and suppresses the excess metal accumulation, which is a medium for phase separation in III-nitride ternary growth. This control is also very effective in suppressing phase separation during ScAlN growth. In a previous study, $\text{Sc}_{0.2}\text{Al}_{0.8}\text{N}$ (close to lattice-matched to GaN) was grown under metal-rich growth conditions having state-of-the-art x-ray diffraction figures of merit with various III/V ratios and substrate temperatures and with an optimized shutter open/closed time.²⁴ The sample in the study was grown at a substrate temperature of 650 °C with a III/V ratio of 1.6 and showed improved film quality in XRD figures of merit, with the (0002) RC showing a FWHM of 229 arc sec. Atomic force microscopy (AFM) showed an RMS roughness of 0.8 nm. However, this film was still so columnar, a problem common in MBE ScAlN synthesis, that RCs for the (10 $\bar{1}$ 5) asymmetric reflection were not measurable with ordinary laboratory equipment. Even so, the HEMT structure consisting of 20 nm of $\text{Sc}_{0.2}\text{Al}_{0.8}\text{N}$ atop unintentionally doped (UID) GaN had the lowest

reported sheet resistance of $152 \Omega/\square$, a mobility of $700 \text{ cm}^2/\text{Vs}$, and a sheet charge of $5.9 \times 10^{13} \text{ cm}^{-2}$, which is close to the theoretical maximum of $6 \times 10^{13} \text{ cm}^{-2}$. There is a report of ScAlN grown by PA-MBE in nitrogen-rich condition with a measured XRD RC for both (0002) symmetric and asymmetric reflection,³³ but their sheet charge ($3.6 \times 10^{13} \text{ cm}^{-2}$) was lower, and their sheet resistance ($233 \Omega/\square$) was higher than our previous report by Engel *et al.*,²⁴ while their mobility ($744 \text{ cm}^2/\text{Vs}$) was higher than our previous report.²⁴ Subsequent optimizations achieved further improvement in the quality $\text{Sc}_{0.18}\text{Al}_{0.82}\text{N}$ films by using the MME technique with a substrate temperature of 400°C ,³⁹ resulting in an XRD (0002) RC FWHM of 250 arcsec , and state-of-the-art RCs for the (10 $\bar{1}$ 5) asymmetric reflection of 469 arcsec as shown in Fig. 2(b). As shown in Fig. 3, both these MME films represent the state of the art compared to the MBE and MOCVD literature and there is a general trend of improving crystal quality as substrate temperature is reduced.^{7,10,24,25,40–43} Growing good-quality films under low substrate temperatures is important for manufacturing uniformity and compatibility with other processes such as CMOS.

Given the similarity of symmetric XRD figures of merit yet dissimilar asymmetric figures of merit along with notably different lattice constants, a thorough structural investigation is crucial for gaining an understanding of metal-rich grown ScAlN films. The structural properties of wurtzite ScAlN grown on GaN remain unclear, and further investigation is important to probe the mechanisms of defect formation and find ways to improve the film quality and corresponding device performance. There are several studies investigating the structural properties of ScAlN grown by RF sputtering, MOCVD, and traditional MBE,^{4,44,45–52,53,54} but none on MME films which show substantially better XRD figures of merit. Since ScN has a rock-salt structure and AlN has a wurtzite structure, it is reported that around a Sc composition of 40%–50%, ScAlN will lose its stability, changing its phase from wurtzite to rock salt, and lose its

piezoelectricity.^{14,48,55} The instability of high scandium ScAlN is reported, with the majority of films having either mixed phase or smaller rock-salt phase inclusions^{14,55} or abnormally oriented grains.^{8,50,52} The present study demonstrates improved-quality ScAlN with an 18% Sc sample grown at a substrate temperature of 400°C showing a lower density of TDs and a 20% Sc sample grown at a substrate temperature of 650°C showing a higher density of threading dislocations (TDs) yet XRD symmetric values comparable to the best in the literature. Tilt, twist, and distorted hexagonal lattice features in the $T_{\text{sub}} = 650^\circ\text{C}$ sample are also revealed herein and can explain the instability of the crystallinity of the ScAlN alloy and further the understanding of the defect mechanisms in ScAlN.

EXPERIMENTAL

Two samples of ScAlN grown at different substrate temperatures, 400 and 650°C , with the same III/V ratio of 1.6 and with a film thickness of 100 nm , are further investigated herein from the growth series of optimization found in the literature.^{24,39} Both films have nominally the same $\sim 19\%$ Sc composition $\pm 1\%$. The $T_{\text{sub}} = 650^\circ\text{C}$ sample from the previous study²⁴ has a composition of $\text{Sc}_{0.20}\text{Al}_{0.80}\text{N}$ and the $T_{\text{sub}} = 400^\circ\text{C}$ sample in the present study has a composition of $\text{Sc}_{0.18}\text{Al}_{0.82}\text{N}$, targeting the approximate (still disputed) lattice match to GaN. We note that according to a fit of the scattered data in Fig. 1 for Sc = 0–31% (considered the most reliable/consistent single-phase data) ScAlN would be lattice-matched to GaN at $\sim 12.0\%$. Given the discrepancy, the lattice constants described by Ambacher *et al.*¹⁶ are used throughout this paper. Both films were grown in a Riber 32 MBE reactor utilizing the MME technique, the details of which can be found elsewhere.^{24,28,29,35,39} Both films were grown on $1 \times 1 \text{ cm}^2$ hydride vapor phase epitaxy (HVPE) UID GaN on sapphire templates manufactured by MSE Supplies. The density of threading dislocations is estimated as less than $5 \times 10^8/\text{cm}^2$ as

25 April 2024 10:41:07

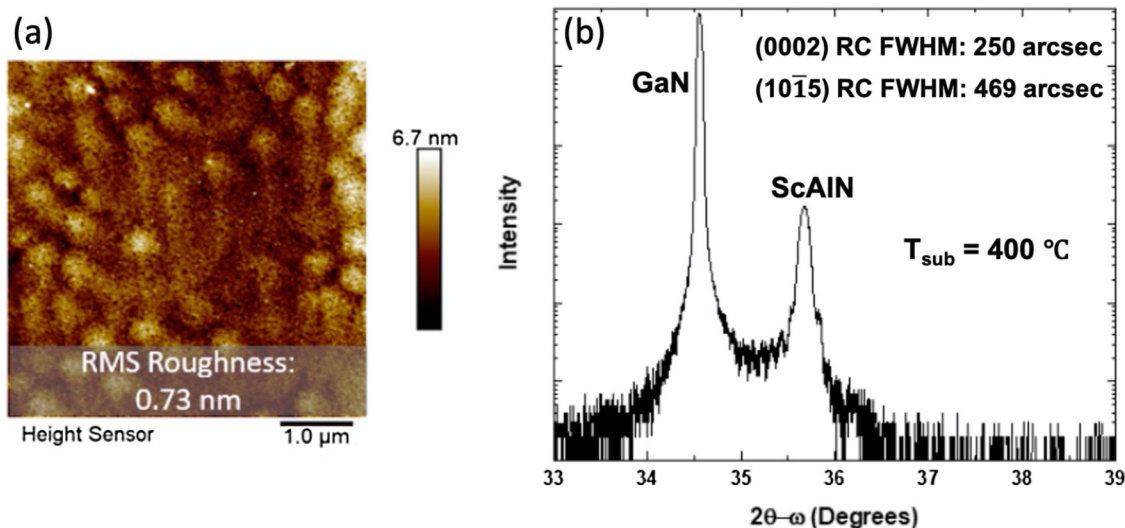


FIG. 2. (a) AFM scan and (b) XRD 2θ - ω scan of the ScAlN film grown under metal-rich conditions at $T_{\text{sub}} = 400^\circ\text{C}$ at a III/V ratio of 1.6.

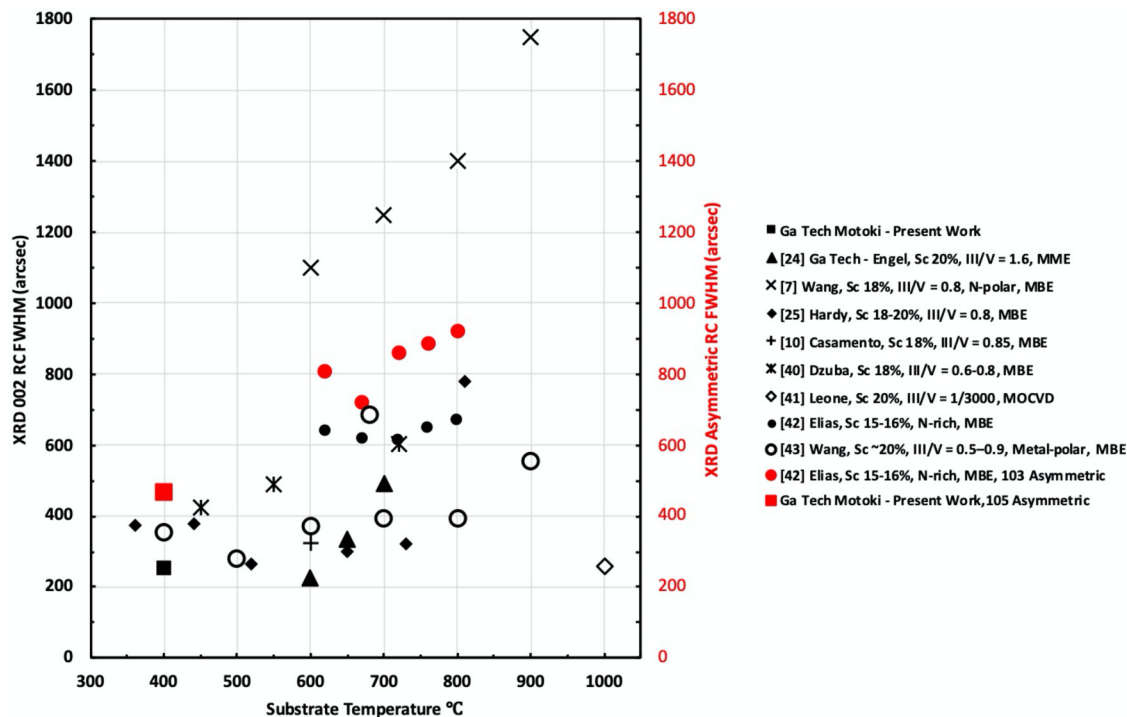


FIG. 3. Survey of literature XRD Rocking Curve width for ScAlN for 15% < Sc < 21% for MBE- and MOCVD-grown films showing a general trend of better quality at lower substrate temperatures. Due to the typical columnar nature of ScAlN, few reports exist for the rocking curve of the asymmetric reflection in MBE- and MOCVD-grown films.^{7,10,24,25,40-43}

reported by the manufacturer. 100-nm-thick GaN was grown to bury the surface contamination and smooth the growth surface before the ScAlN growth. During growth, aluminum and gallium fluxes were provided by conventional effusion cells, and the scandium flux was provided via a high-temperature MBE Komponenten effusion cell. Active nitrogen was provided by a Veeco UNI-Bulb radio frequency (RF) plasma source with an RF power of 350 W and a gas flow of 1.25 SCCM. Because the Sc catalytic decomposition rate of N_2 ²⁴ is temperature dependent, the metal shutter open/closed cycle time was chosen to be 2 s/4 s for $T_{\text{sub}} = 400^\circ\text{C}$ and 2 s/2 s for $T_{\text{sub}} = 650^\circ\text{C}$, and these quick shuttering schemes were chosen to limit the metal adlayer buildup to ~ 1 monolayer for each cycle as determined by RHEED and verified by post-growth film thickness measurements detailed below. This MME shuttering scheme has been implemented in previous studies for growing a series of ScAlN films,³⁹ in addition to AlInN and InGaN films, where the method can limit the adlayer accumulation to 1–1.2 monolayers, preventing vertical segregation and improving the film quality.^{29,30,38} The selected shuttering scheme yields a growth rate of 710 nm/h for GaN and a growth rate of 790 nm/h for ScAlN, as indicated in the literature where an important distinction is higher growth rates when metallic Sc is present on the surface due to the catalytic effect of Sc decomposing N_2 , even plasma excited N_2 .²⁴ While traditional MBE growth will give a global average growth rate by dividing the total film thickness by the total growth time, MME grows only in selected portions of the total shutter cycle

where metal is present, including the portions after the metal shutters are closed (see Ref. 28 for details). Growth in MME occurs while the metal shutters are open and while the metal shutters are closed, and the accumulated metal species is consumed by the active nitrogen. There are portions of time when the shutters are closed that the accumulated metal has been consumed and growth momentarily stops. Thus, the simple global average growth rate is inappropriate in the case of MME. To obtain the appropriate growth rate, the total thickness was measured by a KLA Tencor P15 profilometer by measuring the height difference between the growth surface and the surface underneath regions shadowed by sample holder clips. The instantaneous growth rate, which is valid for the portions of the time in the shutter cycle, was determined by dividing the measured total thickness by the active duty cycle of the growth. The active duty cycle is the ratio of the actual growth time in a cycle ($[\text{shutter open time}] \times [\text{III/V ratio}]$) to the total cycle time ($[\text{shutter open time}] + [\text{shutter closed time}]$). Using this calculation, the growth rate also accounts for the time metal is consumed while the shutters are closed and excludes the time when growth stops while the shutters are still closed.^{24,29} Reflection high energy electron diffraction (RHEED) was used to monitor the growth surface *in situ* to calibrate the III/V ratio and the metal dose.

XRD analysis was performed with a Phillips X'pert Pro MRD using a Cu $K\alpha 1$ anode.^{28,38} In XRD ω measurements, the slit size was 1/4 degree, significantly wider than the measured RC FWHM.

25 April 2024 10:41:07

AFM measurements were performed with a Bruker Icon AFM in tapping mode. The grown films were prepared for the cross-sectional TEM (XTEM) investigation by a Thermo Fisher Helios 5CX focused ion beam (FIB) at cryogenic temperatures. Plan-view TEM samples were prepared by mechanical polishing, followed by dimpling and Ar⁺ ion milling using a Gatan precision ion polishing system (PIPS). A FEI Tecnai F30 super-twin field-emission gun TEM operated at 300 kV was used to acquire the TEM, scanning TEM (STEM), high angle annular dark field (HAADF), and 4D-STEM images. Local lattice constant maps (LLCMs), a.k.a., strain maps were calculated from nano-electron-beam diffraction patterns (DPs) from 4D-STEM data sets, using the Gatan GMS3 software. The 4D-STEM required a 10- μm aperture size to avoid interfacial convolution of the nano-electron-beam DPs. While direct measurement of the actual beam size was not possible in our experimental setup, the beam was estimated to have a 5.1 nm radius based on the diffraction image for the GaN substrate. The pixel step size was set to ~ 1 nm. The calculation method is shown elsewhere.³⁶ X-ray photoelectron spectroscopy (XPS) was implemented to get the surface electronic structural information from the valence band (VB) spectra in both samples by using a Thermo K-Alpha XPS operated with an Al K α (1486 eV) source. Ar⁺ ion etching was performed for 30 s to remove contamination from the surface before XPS spectra were collected. After the etching, the C 1s peak showed no changes, indicating that all the surface contamination was removed.

RESULTS AND DISCUSSION

Figures 2(a) and 2(b) show the AFM scan and the XRD 2θ - ω scan of the ScAlN film grown under metal-rich conditions at $T_{\text{sub}} = 400$ °C, respectively. The same measurements for $T_{\text{sub}} = 650$ °C are published in our previous work.²⁴ The AFM result shows a smooth surface with an RMS roughness of 0.73 nm and additionally shows the presence of spiral hillocks, suggesting that the film was grown in a two-dimensional growth mode common to metal-rich MBE or MME. In the XRD 2θ - ω scan, the left peak is from the underlying GaN and the right peak is from ScAlN. The (0002) RC FWHM of 250 arc sec and the (10 $\bar{1}$ 5) RC FWHM of 469 arc sec demonstrate the state-of-the-art quality of the film. In Fig. 2(b), distinct thickness fringes can be seen around the ScAlN peak, indicating the presence of a smooth interface between ScAlN and GaN for the $T_{\text{sub}} = 400$ °C sample compared to the rougher interface of the $T_{\text{sub}} = 650$ °C sample. To our knowledge, the peak for the RC of the (10 $\bar{1}$ 5) asymmetric reflection has not been reported and was not detectable for $T_{\text{sub}} = 650$ °C, meaning that $T_{\text{sub}} = 400$ °C has better crystallinity. The differences between the XRD 2θ - ω scan in the $T_{\text{sub}} = 400$ °C and $T_{\text{sub}} = 650$ °C samples and the visibility of the peak for the RC of the (10 $\bar{1}$ 5) asymmetric reflection imply that using a lower substrate temperature and longer closed-shutter time for the metal sources from 2 to 4 s improves growth quality. In addition, the c lattice constants measured from XRD revealed large differences between the two samples. By XRD peak calculation, the Sc_{0.20}Al_{0.80}N film grown at 650 °C had a c lattice constant of 4.965 Å, while the Sc_{0.18}Al_{0.82}N film grown at 400 °C had a c lattice constant of 5.027 Å. The theoretical calculation of Ambacher *et al.*¹⁶ determined that the c lattice constant for Sc_{0.20}Al_{0.80}N is 5.022 Å, which is

$\sim 1.14\%$ higher than our experimental results. However, the theoretical c lattice constant calculated for Sc_{0.18}Al_{0.82}N is 5.024 Å, $\sim 0.06\%$ lower than our experimental result, providing a close experiment to theory agreement. Despite the uncertainty in the literature regarding the exact physical parameters used in the modeling and calculations as well as the fact that Rutherford backscattering spectrometry (RBS), energy dispersive X-ray (EDX), and XPS measurements can have some degree of error in determining the composition, the large c lattice constant discrepancy of $\sim 1.14\%$ for Sc_{0.20}Al_{0.80}N grown at 650 °C cannot be explained only by the error of such measurements. Since ScN has a rock-salt (cubic) crystal structure and AlN has a wurtzite (hexagonal) structure, some domains in the overall wurtzite ScAlN may have inclusions of cubic ScAlN or ScN. When the film is grown under a lower temperature, the inclusions could be suppressed, improving the purity of the wurtzite ScAlN, thus improving the crystal quality. The inclusion of cubic domains can induce distortion in the crystal, which could explain the difference in the c lattice constant. In part, the TEM study was intended to support or refute this hypothesis.

Figures 4(a)–4(c) show the XTEM image of the $T_{\text{sub}} = 400$ °C sample taken close to the $1\bar{1}00$ zone axis and dark-field (DF)-XTEM images taken under the two-beam condition of $g = 11\bar{2}0$ and the two-beam condition of $g = 0002$, respectively. Figures 4(d)–4(f) show the XTEM images taken under the same conditions as Figs. 4(a)–4(c), respectively, for the $T_{\text{sub}} = 650$ °C sample. It is noted that the zone axis images will depict contrasts related to any type of dislocations, strain, etc. while the images with $g = 11\bar{2}0$ and $g = 0002$ highlight edge-type and screw-type (or mixed-type) dislocations, respectively, as well as some Moiré fringes related to these vectors. By comparing Figs. 4(a)–4(c) and Figs. 4(d)–4(f), it is evident that (1) each of the ScAlN films is substantially more defective than typical III-nitride semiconductors resulting in complex TEM images; (2) the $T_{\text{sub}} = 400$ °C sample has clearer TD contrast, especially screw/mixed-type dislocations, while the $T_{\text{sub}} = 650$ °C sample has very complex contrasts associated with a large number of dislocations, strains, grains, etc. in each of the three imaging conditions. Clearly, the $T_{\text{sub}} = 650$ °C sample is substantially more columnar than the $T_{\text{sub}} = 400$ °C sample as suggested by the asymmetric XRD results. The features shown in Figs. 4(d)–4(f) indicate that the high-temperature growth induced many defects possibly associated with inclusions of cubic domains, strains, grains, and other crystallographic defects. Notably, the density of screw- and mixed-type TDs in the $T_{\text{sub}} = 400$ °C sample is estimated to be $\sim 4 \times 10^{10} \text{ cm}^{-2}$, much higher than the densities of screw/mixed-type TDs in other III-nitrides such as GaN, AlN, InN, and related ternaries grown with MOCVD or MBE by 1–2 orders of magnitude.^{36,57,58–65,66,67} The TD density was estimated by counting the number of screw-type dislocations (20 screw/mixed-type TDs) over an area of length 520 nm in the TEM image multiplied by the sample foil thickness of 100 nm (roughly estimated with the possibility of a large error in thickness). Neglecting contributions from the angular rotation of the dislocations, the strain surrounding the dislocations, and the broadening of the XRD FWHM due to crystal size and strain induced curvature of the films. Ayers⁶⁸ provided a way to estimate the dislocation density of the crystal from the XRD RC FWHM. Although the XRD RC FWHM at the

25 April 2024, 10:41:07

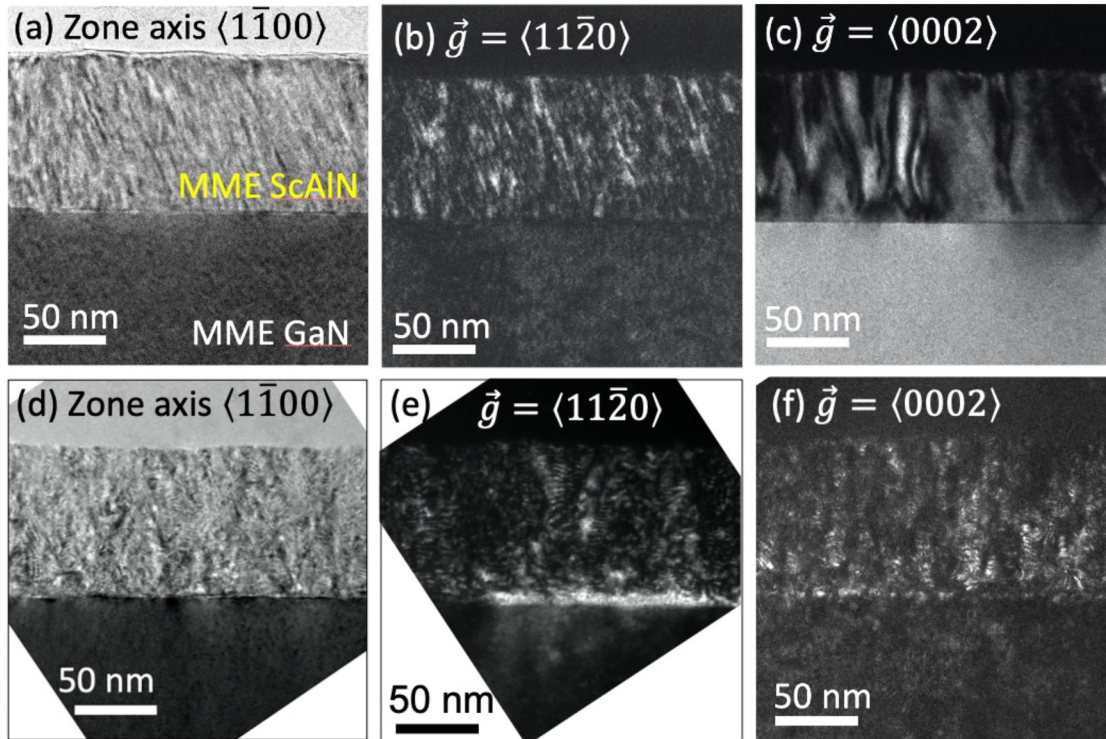


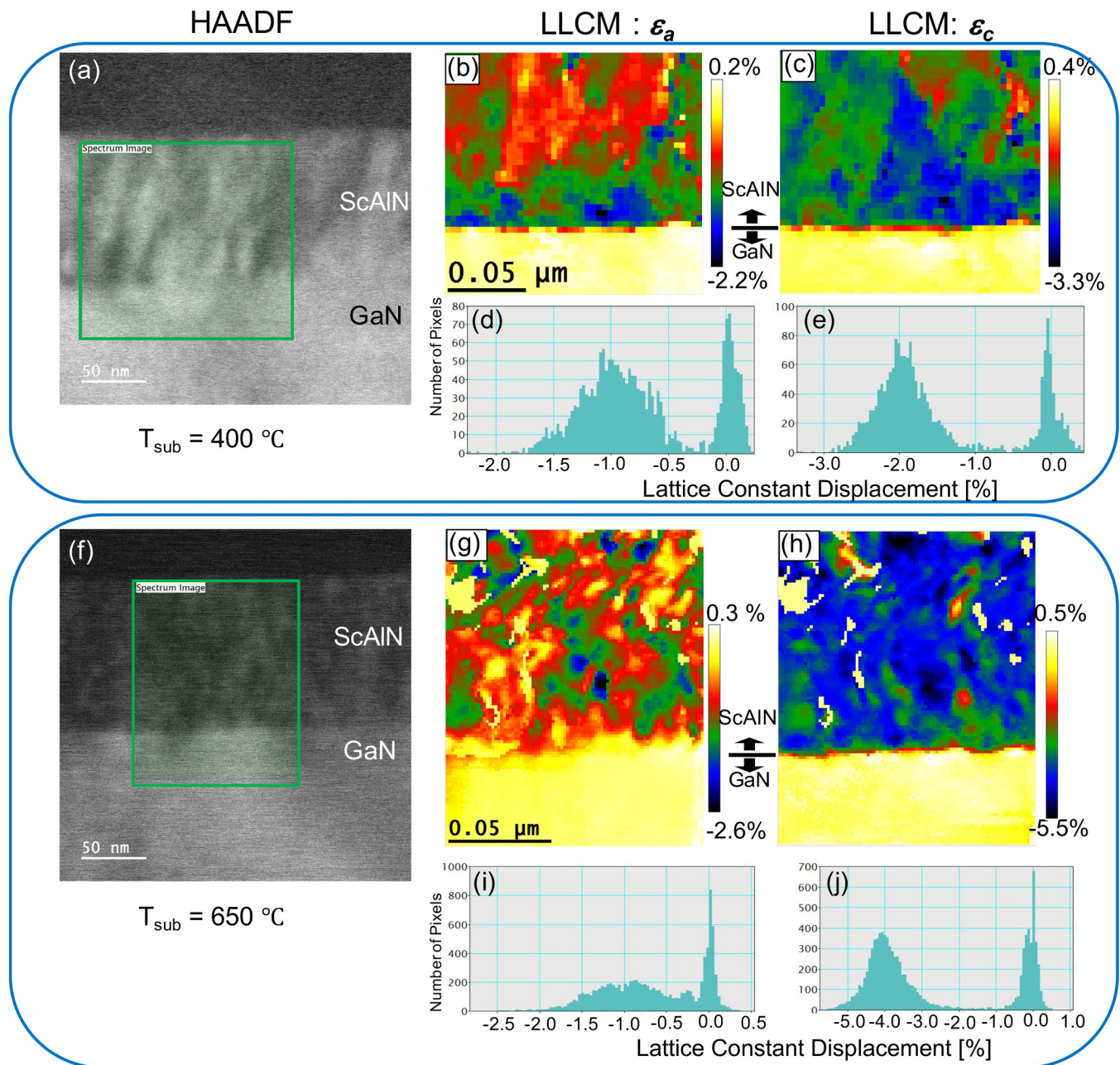
FIG. 4. (a) XTEM image of ScAlN grown at 400 °C taken close to the $\langle 1\bar{1}00 \rangle$ zone axis, (b) DF-XTEM image taken under two-beam condition $\mathbf{g} = 11\bar{2}0$, (c) DF-XTEM image taken under two-beam condition $\mathbf{g} = 0002$, (d) XTEM image of ScAlN film grown at 650 °C taken close to the $\langle 1\bar{1}00 \rangle$ zone axis, (e) DF-XTEM image taken under weak-beam condition $\mathbf{g} = 11\bar{2}0$, and (f) DF-XTEM image taken under two-beam condition $\mathbf{g} = 0002$.

(0002) reflection showed a significantly low value of associated threading dislocation density of $1.34 \times 10^{-8} \text{ cm}^{-2}$, the TEM showed a higher amount of screw and mixed-type dislocations than expected.

A series of LLCMs calculated from 4D-STEM DPs are shown in Fig. 5. Figure 5(a) shows an XSTEM HAADF image for the $T_{\text{sub}} = 400 \text{ °C}$ film and MME-grown GaN. Figure 5(b) shows the LLCM of ϵ_a calculated with respect to the a -lattice constant, $\bar{a} = 1120$, and Fig. 5(c) shows the LLCM of ϵ_c calculated with respect to the c lattice constant, $\bar{c} = 0002$, from 4D-STEM over the square scanned region in Fig. 5(a). Figure 5(d) shows a histogram of the LLCM from Fig. 5(b), and Fig. 5(e) shows a histogram of the LLCM from Fig. 5(c). Comparable data are shown in Figs. 5(f)–5(j) for the ScAlN film grown at $T_{\text{sub}} = 650 \text{ °C}$ and MME-grown GaN. It is noted that although these are traditionally called strain maps, the information presented is the local lattice constant difference referenced from the substrate area, which is GaN in this case. Therefore, the GaN area is mostly shown as $\sim 0\%$. Even though both ScAlN samples are targeted for the approximate a -axis lattice-matched conditions to GaN based on lattice constants of Ambacher *et al.*,¹⁶ both ScAlN films show $\sim -1\%$ a lattice mismatch compared to GaN as shown in Figs. 5(d)–5(i) but with considerably larger scatter in the histogram for the $T_{\text{sub}} = 650 \text{ °C}$ film. Interestingly, while the $T_{\text{sub}} = 400 \text{ °C}$ sample shows abrupt strain relaxation within

$\sim 2 \text{ nm}$ above the ScAlN/GaN interface as shown in Fig. 5(b), we note that the $T_{\text{sub}} = 650 \text{ °C}$ sample shows moderate strain relaxation over the entire ScAlN film in the image. In addition, when comparing the LLCMs of ϵ_c , the histograms shown in Figs. 5(e) and 5(j) the differences in c for the $T_{\text{sub}} = 400$ and 650 °C samples are $\sim -2\%$ and $\sim -4\%$ from GaN, respectively, even though the two films have the same approximate a lattice mismatch. This is consistent with XRD results, especially for the $T_{\text{sub}} = 650 \text{ °C}$ sample, resulting in a c_{ScAlN} at 400 °C of 5.027 Å and a c_{ScAlN} at 650 °C of 4.965 Å , which are $\sim -3.1\%$ and $\sim -4.2\%$ away from the c_{GaN} of 5.185 Å ,⁶⁹ respectively. From the c -lattice constants from both samples, it is evident that the $T_{\text{sub}} = 400 \text{ °C}$ sample has a closer c -lattice constant to the theoretical value of 5.024 Å for $\text{Sc}_{0.18}\text{Al}_{0.82}\text{N}$ than the $T_{\text{sub}} = 650 \text{ °C}$ sample (for $\text{Sc}_{0.20}\text{Al}_{0.80}\text{N}$, c -lattice constant is 5.022 Å) by $\sim 1.1\%$, and this is consistent with our previous measurements from XRD.²⁴ Even with the same approximate a -lattice constant, both samples having different c -lattice constants means that the volume of the crystal is different between the two samples. Considering ScAlN is a ferroelectric material, it is possible to have the crystal shape distorted and have different volumes. There are other reports theorizing the average c -bond difference, bond angle, and distortions dependence on the Sc compositions.^{13,15,70}

As previously mentioned, small columnar grains and cubic inclusions are one interpretation of the TEM for the $T_{\text{sub}} = 650 \text{ °C}$



25 April 2024 10:41:07

FIG. 5. (a) XSTEM HAADF image of the ScAlN film grown at 400 °C on MME-grown GaN, (b) local lattice constant map (LLCM) of ϵ_a ($\bar{a} = 11\bar{2}0$), (c) ϵ_c ($\bar{c} = 0002$) calculated from 4D-STEM over the square scanned region in (a), (d) Histogram of the LLCM in (b), (e) Histogram of the LLCM in (c), (f) XSTEM HAADF image of the ScAlN film grown at 650 °C, (g) LLCM of ϵ_a ($\bar{a} = 11\bar{2}0$), (h) ϵ_c ($\bar{c} = 0002$) calculated from 4D-STEM over the square scanned region in (f), and (i) Histogram of the LLCM in (g), and (j) Histogram of the LLCM in (h).

sample. Additionally, misorientations of the crystal in the local area are also observed. A series of high-resolution local analyses using diffraction patterns extracted from 4D-STEM is shown in Fig. 6. Figure 6(a) shows a 4D-XSTEM DF-HAADF image of ScAlN

grown at $T_{\text{sub}} = 650$ °C. Figures 6(b)–6(d) show local DPs with intensities averaged from the sum of the pixels in each selected area as indicated in (a). In this type of scan, the film is aligned to the ScAlN film, making the intensities in the DPs for ScAlN symmetric

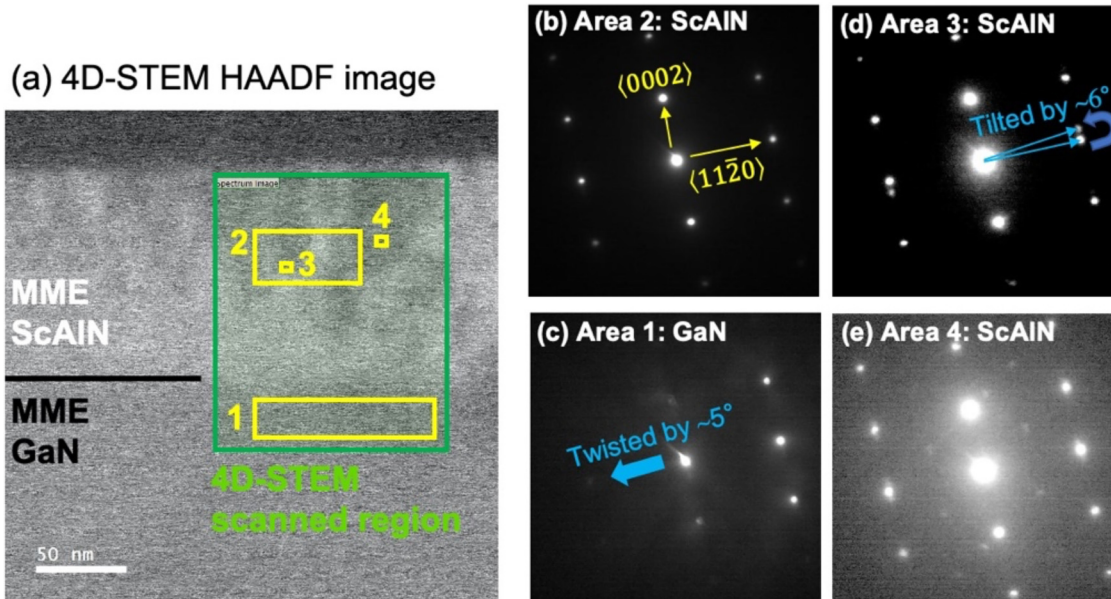


FIG. 6. (a) 4D-XSTEM DF-HAADF image of ScAlN grown at 650 °C and (b)–(d) local DPs from each selected area indicated in (a). Area 1 showed a DP for GaN with asymmetric intensities in the 1120 direction while area 2 showed a DP for ScAlN with symmetric intensities over both the 1120 and the 0002 directions. The DP in area 1 had symmetric intensities after rotating the sample about the 0002 axis by about 5°, which demonstrates the twists of ScAlN from the GaN substrate. Area 3 included a DP with tilted features at about ~6°. Area 4 included multiple points in the DP, indicating the presence of multiple phases of ScAlN.

in both the $1\bar{1}20$ direction and the 0002 direction, as shown in Figs. 6(b)–6(d). Figure 6(b) shows a DP extracted from a reasonably large portion of ScAlN without any obvious anomalies. However, the DPs in the GaN region under the same alignment, as shown in Fig. 5(c), turned out to have asymmetric intensities in the $1\bar{1}20$ direction and symmetric in the 0002 direction, demonstrating that the beam is off the $1\bar{1}00$ zone axis for GaN twisted about the c -axis toward the $1\bar{1}20$ direction. This ScAlN being twisted by $\sim 5^\circ$ from GaN is further confirmed by rotating the sample holder by $\sim 5^\circ$ about the ScAlN c axis, causing the previously asymmetric intensities in the GaN region to become symmetric (not shown). This feature is not detectable during the normal TEM/STEM measurement where the second condenser aperture (C2) is larger, but it is observed in 4D-STEM where the C2 aperture is smaller and more sensitive to the signal variations with position. This suggests that strain in the wurtzite ScAlN crystal is possibly compensated through twisting along the c axis by $\sim 5^\circ$ when growing on wurtzite GaN, a feature not found in other traditional III-Nitrides. This is consistent with the larger number of screw-type threading dislocations observed in Figs. 4(c) and 4(f), where the twisting force generates screw-type dislocations. While these results strictly apply to only higher temperature grown MME films which have improved crystal quality sufficient to observe these local variations, if generalized to ScAlN as a whole, it might imply that the typical small grain structure of ScAlN results from a nanoscale rotational disorder that forces small grain nucleation resulting in columnar growth. Rotations in the $T_{\text{sub}} = 400^\circ\text{C}$ ScAlN film were not observed.

Furthermore, there are some indications of small areas of local crystal tilt in the $T_{\text{sub}} = 650^\circ\text{C}$ ScAlN film, as shown in Fig. 6(d) since there are additional patterns besides the DP spots in $\bar{a} = 1\bar{1}20$ at an angle of $\sim 6^\circ$ from the regular wurtzite DP in a few of the scanned areas. Additionally, Fig. 6(e) implies even more complex patterns in a minority of regions. It is hypothesized that these complex patterns in Fig. 6(d) result from the presence of different phases, possibly suggesting the inclusion of rock-salt domains. While the percentage of local regions containing these non-ideal tilted or multi-phase DPs is small, small enough not to be reflected in the XRD RC figures of merit nor the more global DP for the film shown in Fig. 6(b), these features were not observed at all in the $T_{\text{sub}} = 400^\circ\text{C}$ sample (not shown), which demonstrates that improved film quality and higher crystallographic stability can be achieved at lower substrate temperatures. These tilts and additional phase features are observed only in limited local regions of the $T_{\text{sub}} = 650^\circ\text{C}$ ScAlN film regardless of the minor but perceptible contrasts in the HAADF image shown in Fig. 6(a) because HAADF contrast is less sensitive to crystallographic defects and more sensitive to Z-number.

Further evidence of tilts and twists is revealed in other imaging conditions. Figure 7(a) shows a high-resolution (HR) bright-field (BF) XTEM image of the $T_{\text{sub}} = 650^\circ\text{C}$ sample taken at the $1\bar{1}00$ zone axis. Figure 7(b) shows the fast Fourier transform (FFT)-generated DPs of all areas in Fig. 7(a). Figures 7(c) and 7(d) show FFT-generated DPs over areas 1 and 2 shown in Fig. 7(a), respectively. While there are some regions in Figs. 7(b) and 7(c),

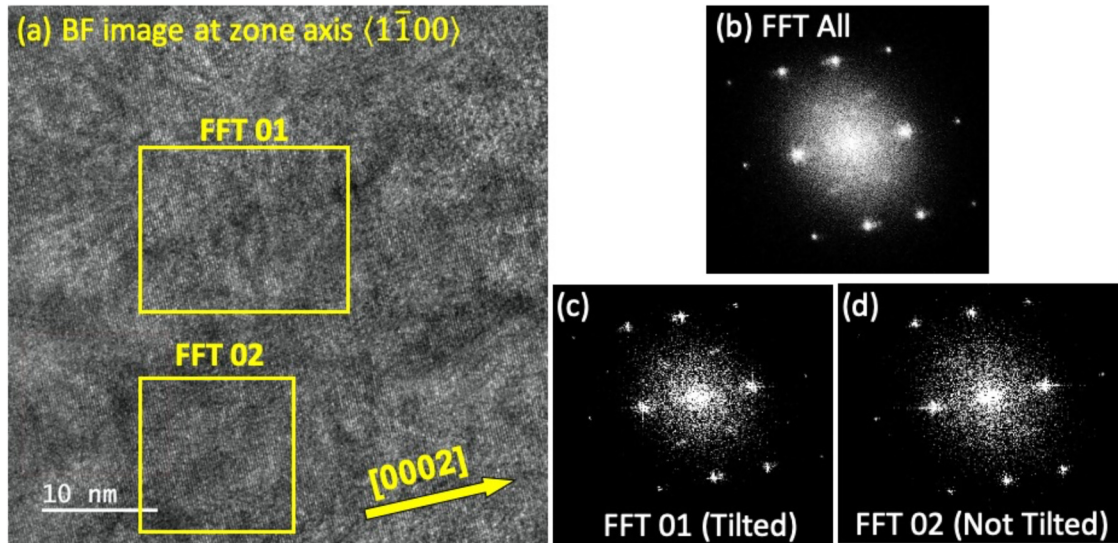


FIG. 7. (a) HR XTEM image of ScAlN grown at 650 °C taken at the $1\bar{1}00$ zone axis, (b) Fast-Fourier Transform (FFT)-generated DP of all areas in (a), and [(c) and(d)] FFT-generated DP over areas 1 and 2, respectively, from the rectangular regions in (a). **Figures 7(b)** and (c) demonstrate the inclusions of tilted DP in addition to the regular DP, while (d) does not show any tilt inclusions.

with spots in $\vec{a} = 11\bar{2}0$ in addition to the regular wurtzite DP, there are other regions like area 2 in **Fig. 7(d)** that show a regular wurtzite DP.

To further examine the rotational distortions in the ScAlN layer, plan-view TEM imaging was performed. **Figure 8(a)** shows a plan-view TEM image of the ScAlN film grown at $T_{\text{sub}} = 400$ °C taken at the 0002 zone axis. **Figure 8(b)** shows a DP taken from (a) using a selective-area aperture. **Figure 8(c)** shows a plan-view TEM image of the ScAlN film grown at $T_{\text{sub}} = 650$ °C taken at the 0002 zone axis. **Figure 8(d)** shows a DP taken from (c) using a selective-area aperture. When comparing **Figs. 8(a)** and **8(c)**, it is evident that the $T_{\text{sub}} = 400$ °C sample has a less complex texture in the real image than the $T_{\text{sub}} = 650$ °C sample. This difference is a result of the $T_{\text{sub}} = 650$ °C sample having more complex defects and a higher defect density than the $T_{\text{sub}} = 400$ °C sample, as seen in the XTEM images in **Fig. 4**. The TD density in the $T_{\text{sub}} = 400$ °C sample counted from the plan-view image is $\sim 6.6 \times 10^{10} \text{ cm}^{-2}$, but the TD density in the $T_{\text{sub}} = 650$ °C sample is uncountable due to the high density of defects and indistinguishable contrasts in the plan-view TEM image. Interestingly, the DP from the $T_{\text{sub}} = 400$ °C sample shows the sharp pattern of a regular hexagon as shown in **Fig. 8(b)**, while the $T_{\text{sub}} = 650$ °C sample shows a streaky pattern with distortion in both the spot elongation and angular positions of the spots, as shown in **Fig. 8(d)**. This DP spot streakiness is evidence of rotational disorder in ScAlN. The degree of distortion in the streak is $\sim 6^\circ$, which is in good agreement with the $\sim 5^\circ$ twist about the c -axis found in the 4D-STEM result shown in **Fig. 6**. The hexagon in the DP is also distorted in one direction as the angle between the center spots and the vertices of the hexagon is not 60° for the $T_{\text{sub}} = 650$ °C sample. For example, the two angles between

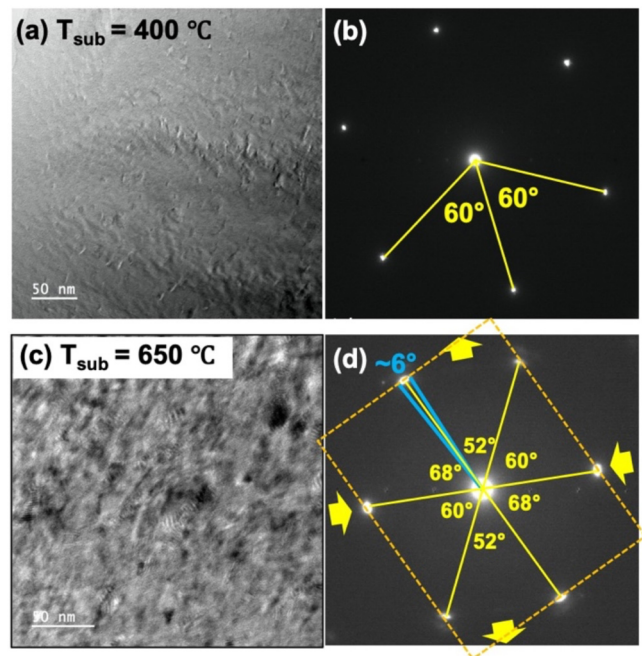


FIG. 8. (a) Plan-view TEM image of the ScAlN film grown at 400 °C taken at the 0002 zone axis, (b) DP taken from (a) using selective-area aperture, indicating symmetric hexagonal pattern, (c) plan-view TEM image of the ScAlN film grown at 650 °C taken at the 0002 zone axis, and (d) DP taken from (c) using selective-area aperture, indicating inclusions of $\sim 6^\circ$ twists and a distorted hexagonal pattern.

25 April 2024 10:41:07

the center spot and two of the vertices of the hexagon, indicated in Fig. 8(d), are 52° and 68° , which differs greatly from the expected angle of 60° for a regular hexagon by $\pm 8^\circ$. This distortion demonstrates that ScAlN can be grown under rotationally distorted conditions on a GaN substrate but seems to be alleviated for the low growth temperature of 400°C . This rotational distortion is also consistent with some other reports describing ScAlN distortions and how changes occur in the bond lengths and angles for ScAlN but not the other III-nitrides.^{13,15,70} A similar phenomenon is reported when GaN is grown on orthorhombic LiGaO₂, and due to the anisotropic strain as observed in XRD, there is an increase and decrease in *a*- and *b*-lattice constant, respectively, forcing a slight rotation about the *c*-axis.⁷¹ Deformation of the hexagon in the plan is theorized, making an orthorhombic crystal structure which is a slightly distorted version of the hexagonal.⁷¹ A similar phenomenon is suggested here for the $T_{\text{sub}} = 650^\circ\text{C}$ sample from the distorted hexagon in the plan-view DP. The twisting feature from the plan-view DP in $T_{\text{sub}} = 650^\circ\text{C}$ sample also supports the previous suggestion that the higher density of screw- and mixed-type dislocations found in ScAlN compared to other III-nitrides can result from the twisting force when ScAlN is grown on GaN. It is also shown that growing ScAlN at the lower substrate temperature of 400°C can improve film quality without introducing distortion and twist features. To gain more understanding, future work will need to examine a wide variety of thicknesses and growth temperatures to determine if these rotations and rotational distortions are relaxations of a rotationally strained crystal or a new phase of ScAlN not previously observed.

Since the electronic structure is coupled to the geometric structure and since for ScAlN, there is a distortion of the geometric structure, the difference in the electronic structure between the two ScAlN samples is also investigated. Figure 9 shows the XPS VB spectra comparing films grown at $T_{\text{sub}} = 400$ and 650°C . The black solid line shows the spectra for the $T_{\text{sub}} = 400^\circ\text{C}$ sample, and the green solid line shows the spectra for the $T_{\text{sub}} = 650^\circ\text{C}$ sample. The dashed lines are extrapolations to the VB edges. The VB levels for the $T_{\text{sub}} = 400^\circ\text{C}$ sample and the $T_{\text{sub}} = 650^\circ\text{C}$ sample are found to be 2.14 and 4.80 eV, respectively. The binding energy of the VB spectra was referenced to C 1s spectra for both samples. In general, SIMS of carbon in MME-grown AlScN is well below $\sim 10^{18}\text{ cm}^{-3}$. While this is much higher than in other MME-grown materials, it is far lower than should be detected by XPS. Thus, we assume the C remaining in XPS after sputtering is related to a source of C inside the XPS system and does not originate from the film. The 2.66 eV difference in the VB levels of the two samples could be caused by a Fermi-level difference, where the VB edge level shows the depth from the Fermi level suggesting a difference in the residual electron concentrations of the unintentionally doped films. The large Fermi-level shift is consistent with a large, unintentional Fermi-energy difference due to the residual electron doping by the exponentially increased concentration of nitrogen vacancies caused by the higher growth temperature.⁷² The Fermi-energy shift cannot be due to sample charging since the sample was grounded with this being verified by no difference in the core spectra.⁷³ There are a few reports of XPS VB spectra for ScAlN, and energy shifts are seen when comparing pure ScAlN and oxidized ScAlN.^{54,74} These reports compared the XPS VB spectra of ScAlN

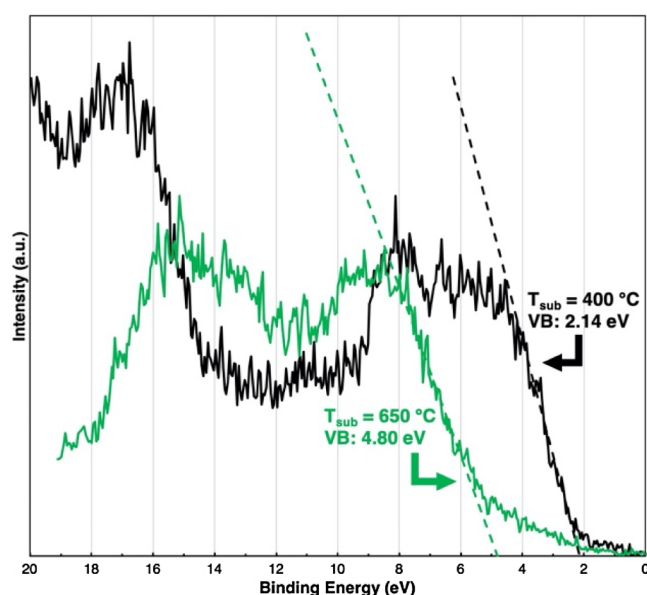


FIG. 9. XPS valence band (VB) spectra comparing the $T_{\text{sub}} = 400^\circ\text{C}$ and $T_{\text{sub}} = 650^\circ\text{C}$ samples. The tail from the extrapolation at the VB edge is broader for the $T_{\text{sub}} = 650^\circ\text{C}$ sample, indicating that the film has lower quality with more crystal disorder than the $T_{\text{sub}} = 400^\circ\text{C}$ sample.

and oxidized ScAlN and found different amounts of energy shifts in the VB edge, but not a shift as large as 2.66 eV.^{54,74} It is possible that the sample grown at 650°C may contain more native defects and/or impurities, perhaps due to more nitrogen vacancies from higher temperatures or more impurities due to hotter effusion cells and the substrate heater. We also cannot rule out the possibility that the films could have oxidized over time from keeping the samples in the atmosphere at room temperature as reported elsewhere.^{54,74} However, both samples were grown and then exposed to the atmosphere for 8–10 months prior to the XPS measurement, and the VB spectrum of the $T_{\text{sub}} = 400^\circ\text{C}$ sample more closely matched what has been reported as non-oxidized ScAlN.^{54,74} Additionally, the tail from the extrapolation at the VB edge is broader for the $T_{\text{sub}} = 650^\circ\text{C}$ sample, indicating more disorder in the crystal structure because of the lower quality of the film.^{75–77} However, the $T_{\text{sub}} = 400^\circ\text{C}$ sample does not show significant VB tailing, and thus, the film is grown with minimal crystal disorder, making it a higher electronic quality sample than its $T_{\text{sub}} = 650^\circ\text{C}$ counterpart.

CONCLUSION

In this study, ScAlN with an 18% Sc composition and state-of-the-art x-ray diffraction figures of merit was grown directly on GaN using MME. Growing metal rich (III/V = 1.6) and at a low substrate temperature of 400°C produced a film with state-of-the-art crystal quality. The improved quality is exhibited via a (0002) XRD RC FWHM of 250 arc sec, a (10 $\bar{1}$ 5) XRD RC FWHM of 469 arc sec, and a smooth surface with an RMS roughness of 0.73 nm. The

25 April 2024 10:41:07

structural properties of the $T_{\text{sub}} = 400\text{ }^{\circ}\text{C}$ and $T_{\text{sub}} = 650\text{ }^{\circ}\text{C}$ samples are also compared via TEM and 4D-STEM with the $T_{\text{sub}} = 400\text{ }^{\circ}\text{C}$ sample having a lower TD density but both showed screw- and mixed-type TDs common in ScAlN, a unique feature among III-nitrides that typically have low screw- and mixed-type TD densities. LCM histograms and XRD indicated that the $T_{\text{sub}} = 400\text{ }^{\circ}\text{C}$ sample has a c lattice constant about 2% greater than that of the $T_{\text{sub}} = 650\text{ }^{\circ}\text{C}$ sample and closer to the theoretical value and despite both films being close to the 18–20% Sc range literature suggests is needed to lattice match to GaN, their relaxed lattice constants were substantially different from that of GaN possibly implying the lattice match to GaN occurs at lower compositions than commonly accepted. Significant tilts and twists are also found in the $T_{\text{sub}} = 650\text{ }^{\circ}\text{C}$ sample by XTEM, 4D-STEM, and plan-view TEM, which are not commonly found in the III-nitrides, and are crucial for understanding the defect mechanisms within the ScAlN alloy. The high number of screw-type TDs and an orthorhombic diffraction pattern (distorted hexagon) in the plan-view TEM are evidence of a twisting force in ScAlN grown on GaN and may originate from the reduction in rotational rigidity due to fewer valence s-p coordinated bonds when introducing Scandium's d-electrons into the valence bonds. XPS revealed improved electronic spectral densities for the $T_{\text{sub}} = 400\text{ }^{\circ}\text{C}$ sample. The present study provides a pathway to low-temperature synthesis and possible CMOS compatibility, while providing a greater understanding of the complicated structural properties of ScAlN, aiming to improve device performance by better understanding how to control defects.

ACKNOWLEDGMENTS

This work was supported by the Office of Naval Research (ONR) Multidisciplinary University Research Initiatives (MURI) program entitled, "Leveraging a New Theoretical Paradigm to Enhance Interfacial Thermal Transport In Wide Bandgap Power Electronics" under Award No. N00014-17-S-F006 administered by Dr. Mark Spector and Capt. Lynn Petersen. This work is also supported by the Defense Advanced Research Project Agency (DARPA) program entitled, "Multilayer Molecular-Beam Epitaxy Stacks with Intermetallic Layers Enabled Bulk Acoustic Resonators (MM-BAR)" under Award No. HR001121S0031 administered by Dr. Benjamin Griffin. Any opinions, findings, conclusions, or recommendations expressed in this material are those of the author(s) and do not necessarily reflect those of the ONR or DARPA. The authors would also like to thank Dr. Yong Ding and Dr. Mengkun Tian who assisted in TEM and STEM.

AUTHOR DECLARATIONS

Conflict of Interest

The authors have no conflicts to disclose.

Author Contributions

Keisuke Motoki: Conceptualization (equal); Data curation (equal); Formal analysis (equal); Investigation (equal); Methodology (equal); Visualization (equal); Writing – original draft (equal).
Zachary Engel: Conceptualization (supporting); Data curation

(supporting); Formal analysis (equal); Investigation (equal); Methodology (equal); Visualization (equal); Writing – review & editing (equal). **Timothy M. McCrone:** Data curation (equal); Formal analysis (equal); Investigation (equal). **Huijin Chung:** Investigation (supporting). **Christopher M. Matthews:** Data curation (supporting); Investigation (supporting); Methodology (supporting); Writing – review & editing (supporting). **Sangho Lee:** Data curation (supporting); Investigation (supporting). **Emily N. Marshall:** Conceptualization (supporting); Data curation (supporting); Investigation (supporting); Methodology (supporting); Writing – review & editing (equal). **Aheli Ghosh:** Data curation (supporting); Formal analysis (supporting); Investigation (supporting); Writing – review & editing (equal). **Amanda Tang:** Data curation (supporting); Formal analysis (supporting); Investigation (supporting); Methodology (supporting); Writing – review & editing (supporting). **W. Alan Doolittle:** Conceptualization (equal); Data curation (equal); Formal analysis (equal); Funding acquisition (equal); Investigation (equal); Methodology (equal); Project administration (equal); Resources (equal); Supervision (equal); Validation (equal); Visualization (equal); Writing – review & editing (equal).

DATA AVAILABILITY

The data that support the findings of this study are available from the corresponding author upon reasonable request.

REFERENCES

- 1K. Furuta, K. Hirata, S. A. Anggraini, M. Akiyama, M. Uehara, and H. Yamada, *J. Appl. Phys.* **130**, 024104 (2021).
- 2D. Wang, P. Wang, S. Mondal, S. Mohanty, T. Ma, E. Ahmadi, and Z. Mi, *Adv. Electron. Mater.* **8**, 2200005 (2022).
- 3P. Wang, D. Wang, N. M. Vu, T. Chiang, J. T. Heron, and Z. Mi, *Appl. Phys. Lett.* **118**, 223504 (2021).
- 4N. Wolff, S. Fichtner, B. Haas, M. R. Islam, F. Niekkel, M. Kessel, O. Ambacher, C. Koch, B. Wagner, F. Lofink, and L. Kienle, *J. Appl. Phys.* **129**, 034103 (2021).
- 5R. Deng, *Aluminum Nitride, Scandium Nitride, and Aluminum-Scandium-Nitride Ternary Alloys: Structural, Optical, and Electrical Properties* (Rensselaer Polytechnic Institute PP, New York, 2013).
- 6P. M. Mayrhofer, C. Eisenmenger-Sittner, M. Stöger-Pollach, H. Euchner, A. Bittner, and U. Schmid, *J. Appl. Phys.* **115**, 193505 (2014).
- 7P. Wang, D. Wang, B. Wang, S. Mohanty, S. Diez, Y. Wu, Y. Sun, E. Ahmadi, and Z. Mi, *Appl. Phys. Lett.* **119**, 082101 (2021).
- 8M. T. Hardy, E. N. Jin, N. Nepal, D. S. Katzer, B. P. Downey, V. J. Gokhale, D. F. Storm, and D. J. Meyer, *Appl. Phys. Express* **13**, 065509 (2020).
- 9R. Dargis, A. Clark, A. Ansari, Z. Hao, M. Park, D. Kim, R. Yanka, R. Hammond, M. Debnath, and R. Pelzel, *Phys. Status Solidi* **217**, 1900813 (2020).
- 10J. Casamento, C. S. Chang, Y.-T. Shao, J. Wright, D. A. Muller, H. (Grace) Xing, and D. Jena, *Appl. Phys. Lett.* **117**, 112101 (2020).
- 11S. Fichtner, N. Wolff, G. Krishnamurthy, A. Petraru, S. Bohse, F. Lofink, S. Chemnitz, H. Kohlstedt, L. Kienle, and B. Wagner, *J. Appl. Phys.* **122**, 035301 (2017).
- 12D. Wang, P. Wang, S. Mondal, Y. Xiao, M. Hu, and Z. Mi, *Appl. Phys. Lett.* **121**, 042108 (2022).
- 13N. Kurz, A. Ding, D. F. Urban, Y. Lu, L. Kirste, N. M. Feil, A. Žukauskaitė, and O. Ambacher, *J. Appl. Phys.* **126**, 075106 (2019).
- 14M. Akiyama, T. Kamohara, K. Kano, A. Teshigahara, Y. Takeuchi, and N. Kawahara, *Adv. Mater.* **21**, 593 (2009).

25 April 2024 10:41:07

- ¹⁵D. F. Urban, O. Ambacher, and C. Elsässer, *Phys. Rev. B* **103**, 115204 (2021).
- ¹⁶O. Ambacher, B. Christian, M. Yassine, M. Baeumler, S. Leone, and R. Quay, *J. Appl. Phys.* **129**, 204501 (2021).
- ¹⁷O. Ambacher, B. Christian, N. Feil, D. F. Urban, C. Elsässer, M. Prescher, and L. Kirste, *J. Appl. Phys.* **130**, 045102 (2021).
- ¹⁸K. Frei, R. Trejo-Hernández, S. Schütt, L. Kirste, M. Prescher, R. Aidam, S. Müller, P. Waltereit, O. Ambacher, and M. Fiederle, *Jpn. J. Appl. Phys.* **58**, SC1045 (2019).
- ¹⁹J. Yang, X. Meng, C. Yang, and Y. Zhang, *Appl. Surf. Sci.* **287**, 355 (2013).
- ²⁰Y. Zhang, W. Zhu, D. Zhou, Y. Yang, and C. Yang, *J. Mater. Sci. Mater. Electron.* **26**, 472 (2015).
- ²¹M. Akiyama, K. Kano, and A. Teshigahara, *Appl. Phys. Lett.* **95**, 162107 (2009).
- ²²M. B. Tahhan, J. A. Logan, M. T. Hardy, M. G. Ancona, B. Schultz, B. Appleton, T. Kazior, D. J. Meyer, and E. M. Chumbes, *IEEE Trans. Electron Devices* **69**, 962 (2022).
- ²³M. Sumisaka, K. Yamazaki, S. Fujii, G. Tang, T. Han, Y. Suzuki, S. Otomo, T. Omori, and K. Hashimoto, *Jpn. J. Appl. Phys.* **54**, 07HD06 (2015).
- ²⁴Z. Engel, K. Motoki, C. M. Matthews, and W. A. Doolittle, *J. Appl. Phys.* **132**, 185302 (2022).
- ²⁵M. T. Hardy, B. P. Downey, N. Nepal, D. F. Storm, D. S. Katzer, and D. J. Meyer, *Appl. Phys. Lett.* **110**, 162104 (2017).
- ²⁶M. Hardy, D. Meyer, N. Nepal, B. Downey, D. S. Katzer, and D. Storm, in *2018 IEEE MTT-S International Microwave Workshop Series on Advanced Materials and Processes for RF and THz Applications* (IEEE, 2018), pp. 1–3.
- ²⁷T. E. Kazior, E. M. Chumbes, B. Schultz, J. Logan, D. J. Meyer, and M. T. Hardy, in *2019 IEEE MTT-S International Microwave Symposium* (IEEE, 2019), pp. 1136–1139.
- ²⁸H. Ahmad, K. Motoki, E. A. Clinton, C. M. Matthews, Z. Engel, and W. A. Doolittle, *ACS Appl. Mater. Interfaces* **12**, 37693 (2020).
- ²⁹Z. Engel, E. A. Clinton, C. M. Matthews, and W. A. Doolittle, *J. Appl. Phys.* **127**, 125301 (2020).
- ³⁰M. Moseley, J. Lowder, D. Billingsley, and W. A. Doolittle, *Appl. Phys. Lett.* **97**, 191902 (2010).
- ³¹S.-Y. Kwon, H. J. Kim, H. Na, Y.-W. Kim, H.-C. Seo, H. J. Kim, Y. Shin, E. Yoon, and Y.-S. Park, *J. Appl. Phys.* **99**, 044906 (2006).
- ³²F. Widmann, B. Daudin, G. Feuillet, N. Pelekanos, and J. L. Rouvière, *Appl. Phys. Lett.* **73**, 2642 (1998).
- ³³P. Wang, D. Wang, Y. Bi, B. Wang, J. Schwartz, R. Hovden, and Z. Mi, *Appl. Phys. Lett.* **120**, 012104 (2022).
- ³⁴M. Moseley, J. Lowder, D. Billingsley, and W. A. Doolittle, *Appl. Phys. Lett.* **97**, 70 (2010).
- ³⁵Z. Engel, E. A. Clinton, K. Motoki, H. Ahmad, C. M. Matthews, and W. A. Doolittle, *J. Appl. Phys.* **130**, 165304 (2021).
- ³⁶E. A. Clinton, Z. Engel, E. Vadiée, J. V. Carpenter, Z. C. Holman, and W. A. Doolittle, *Appl. Phys. Lett.* **115**, 082104 (2019).
- ³⁷K. Motoki, Z. Engel, C. M. Matthews, H. Ahmad, T. M. McCrone, K. Harada, and W. A. Doolittle, *J. Vac. Sci. Technol. B* **40**, 052210 (2022).
- ³⁸M. Moseley, B. Gunning, J. Greenlee, J. Lowder, G. Namkoong, and W. Alan Doolittle, *J. Appl. Phys.* **112**, 014909 (2012).
- ³⁹Z. Engel, *Controlling Adatom Kinetics to Overcome Traditional Limitations for III-Nitride Ternary Alloys* (Georgia Institute of Technology, 2022).
- ⁴⁰B. Dzuba, T. Nguyen, A. Sen, R. E. Diaz, M. Dubey, M. Bachhav, J. P. Wharry, M. J. Manfra, and O. Malis, *J. Appl. Phys.* **132**, 175701 (2022).
- ⁴¹S. Leone, J. Ligl, C. Manz, L. Kirste, T. Fuchs, H. Menner, M. Prescher, J. Wiegert, A. Žukauskaitė, R. Quay, and O. Ambacher, *Phys. Status Solidi – Rapid Res. Lett.* **14**, 1900535 (2020).
- ⁴²C. Elias, M. Nemoz, H. Rotella, F. Georgi, S. Vézian, M. Hugues, and Y. Cordier, *APL Mater.* **11**, 031105 (2023).
- ⁴³P. Wang, D. A. Laleyan, A. Pandey, Y. Sun, and Z. Mi, *Appl. Phys. Lett.* **116**, 151903 (2020).
- ⁴⁴D. K. T. Ng, C.-P. Ho, T. Zhang, L. Xu, L.-Y. Siow, W.-W. Chung, H. Cai, L. Y. T. Lee, Q. Zhang, and N. Singh, *Proc. SPIE* **11697**, 116970N (2021).
- ⁴⁵M. Li, K. Hu, H. Lin, and Y. Zhu, in *IEEE International Ultrasonics Symposium IUS 2021* (IEEE, 2021).
- ⁴⁶C. Höglund, B. Alling, J. Birch, M. Beckers, P. O. Persson, C. Baetz, Z. Czigány, J. Jensen, and L. Hultman, *Phys. Rev. B: Condens. Matter Mater. Phys.* **81**, 224101 (2010).
- ⁴⁷P. H. Chen, S. Wu, Y. C. Chen, J. L. Huang, D. F. Lii, and Z. X. Lin, *Surf. Coat. Technol.* **284**, 129 (2015).
- ⁴⁸S. Fujii, M. Sumisaka, G. Tang, Y. Suzuki, S. Otomo, T. Omori, and K. Y. Hashimoto, in *2015 IEEE MTT-S International Microwave Symposium (IMS)* (IEEE, 2015), Vol. 2015, p. 1.
- ⁴⁹A. Qamar, H. P. Phan, T. Dinh, N. T. Nguyen, and M. Rais-Zadeh, *Appl. Phys. Lett.* **116**, 132902 (2020).
- ⁵⁰M. Li, J. Xie, B. Chen, N. Wang, and Y. Zhu, in *IEEE International Ultrasonics Symposium (IUS), 2019 October* (IEEE, 2019), p. 1124.
- ⁵¹S. Kerdsonpanya, N. Van Nong, N. Pryds, A. Žukauskaite, J. Jensen, J. Birch, J. Lu, L. Hultman, G. Wingqvist, and P. Eklund, *Appl. Phys. Lett.* **99**, 232113 (2011).
- ⁵²C. S. Sandu, F. Parsapour, S. Mertin, V. Pashchenko, R. Matloub, T. LaGrange, B. Heinz, and P. Murali, *Phys. Status Solidi A* **216**, 1800569 (2019).
- ⁵³P. Musavigharavi, A. C. Meng, D. Wang, J. Zheng, A. C. Foucher, R. H. Olsson, and E. A. Stach, *J. Phys. Chem. C* **125**, 14394 (2021).
- ⁵⁴M. Li, H. Lin, K. Hu, and Y. Zhu, *Appl. Phys. Lett.* **121**, 111602 (2022).
- ⁵⁵A. Teshigahara, K. Hashimoto, and M. Akiyama, in *2012 IEEE International Ultrasonics Symposium* (IEEE, 2012), pp. 1–5.
- ⁵⁶Y. Ding, Y. M. Choi, Y. Chen, K. C. Pradel, M. Liu, and Z. L. Wang, *Mater. Today* **38**, 24 (2020).
- ⁵⁷J. W. P. Hsu, M. J. Manfra, S. N. G. Chu, C. H. Chen, L. N. Pfeiffer, and R. J. Molnar, *Appl. Phys. Lett.* **78**, 3980 (2001).
- ⁵⁸B. Heying, E. J. Tarsa, C. R. Elsass, P. Fini, S. P. DenBaars, and J. S. Speck, *J. Appl. Phys.* **85**, 6470 (1999).
- ⁵⁹J. W. P. Hsu, M. J. Manfra, R. J. Molnar, B. Heying, and J. S. Speck, *Appl. Phys. Lett.* **81**, 79 (2002).
- ⁶⁰C. Kruse, H. Dartsch, T. Aschenbrenner, S. Figge, and D. Hommel, *Phys. Status Solidi* **248**, 1748 (2011).
- ⁶¹I. Gherasoiu, M. O’Steen, T. Bird, D. Gotthold, A. Chandolu, D. Y. Song, S. X. Xu, M. Holtz, S. A. Nikishin, and W. J. Schaff, *Phys. Status Solidi C* **5**, 1642 (2008).
- ⁶²N. Izyumskaya, V. Avrutin, K. Ding, Özgür, H. Morkoç, and H. Fujioka, *Semicond. Sci. Technol.* **34**, 093003 (2019).
- ⁶³A. Yoshikawa, S. Che, Y. Ishitani, and X. Wang, *J. Cryst. Growth* **311**, 2073 (2009).
- ⁶⁴B. Liu, R. Zhang, Z. L. Xie, H. Lu, Q. J. Liu, Z. Zhang, Y. Li, X. Q. Xiu, P. Chen, P. Han, S. L. Gu, Y. Shi, Y. D. Zheng, and W. J. Schaff, *J. Appl. Phys.* **103**, 023504 (2008).
- ⁶⁵P. Ruterana, A. L. Syrkin, E. Monroy, E. Valcheva, and K. Kirilov, *Phys. Status Solidi C* **7**, 1301 (2010).
- ⁶⁶S. I. Petrov, A. N. Alexeev, D. M. Krasovitsky, and V. P. Chaly, *Phys. Status Solidi C* **9**, 562 (2012).
- ⁶⁷D. V. Nechaev, P. A. Aseev, V. N. Jmerik, P. N. Brunkov, Y. V. Kuznetsova, A. A. Sitnikova, V. V. Ratnikov, and S. V. Ivanov, *J. Cryst. Growth* **378**, 319 (2013).
- ⁶⁸J. E. Ayers, *J. Cryst. Growth* **135**, 71 (1994).
- ⁶⁹W. Shan, R. J. Hauenstein, A. J. Fischer, and J. J. Song, *Phys. Rev. B* **54**, 13460 (1996).
- ⁷⁰J. Casamento, H. Lee, T. Maeda, V. Gund, K. Nomoto, L. van Deurzen, W. Turner, P. Fay, S. Mu, C. G. Van de Walle, A. Lal, H. (Grace) Xing, and D. Jena, *Appl. Phys. Lett.* **120**, 152901 (2022).
- ⁷¹G. Namkoong, S. Huang, M. Moseley, and W. A. Doolittle, *Thin Solid Films* **517**, 6508 (2009).

⁷²M. Ohring, *Materials Science of Thin Films, Deposition and Structure, 2nd Edition* (Academic Press, New York, 2001).

⁷³S. Oswald and S. Baunack, *Surf. Interface Anal.* **25**, 942 (1997).

⁷⁴D. Wang, D. Wang, P. Zhou, M. Hu, J. Liu, S. Mondal, T. Ma, P. Wang, and Z. Mi, *Appl. Surf. Sci.* **628**, 157337 (2023).

⁷⁵A. Lotnyk, D. Poppitz, U. Ross, J. W. Gerlach, F. Frost, S. Bernütz, E. Thelander, and B. Rauschenbach, *Microelectron. Reliab.* **55**, 2119 (2015).

⁷⁶Q. Kang, J. Cao, Y. Zhang, L. Liu, H. Xu, and J. Ye, *J. Mater. Chem. A* **1**, 5766 (2013).

⁷⁷S. A. Ansari and M. H. Cho, *Sci. Rep.* **6**, 25405 (2016).